Published in "Nature Materials 8: 315-319, 2009"
which should be cited to refer to this work.

Giant superconductivity-induced modulation of the ferromagnetic magnetization in a cuprate-manganite superlattice

Supporting Material

(Dated: January 22, 2009)

FUNDAMENTALS OF POLARISED NEUTRON REFLECTOMETRY (PNR)

In specular reflectometry one measures how the intensity of a neutron beam that is reflected from a surface (or interface) varies as a function of the momentum transfer normal to the surface q_z. For typical neutron wavelengths of fractions of nm the angle of incidence is of the order of a degree (gracing incidence). Due to their relatively weak interaction with most materials, the probe depth of neutrons is of the order of μm. Accordingly, even burried interfaces usually contribute to the reflectivity signal. Figure 1 shows a sketch of the geometry of a reflectometry set-up and gives an explanation of the used variables.

PNR can be regarded as an analog to optical refraction at interfaces by introducing an

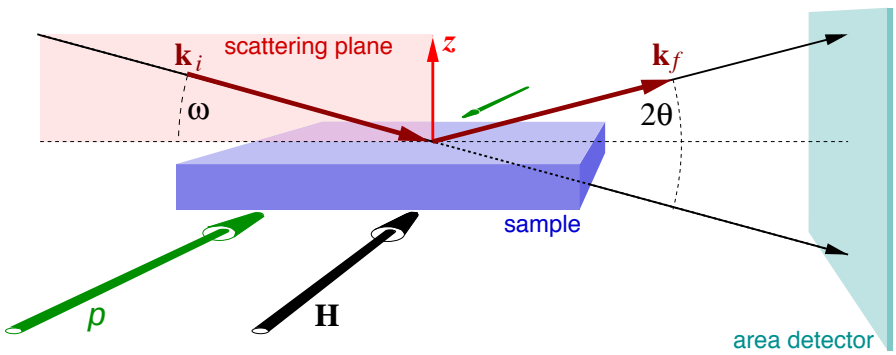

FIG. 1: Sketch of the geometry of the beams and fields for the neutron reflectometry measurements. The scattering plane is spanned by the incident beam $\mathbf{k}_i$ and the final beam $\mathbf{k}_f$ and contains the surface normal $\mathbf{z}$. The angle of incidence relative to the (averaged) surface is denoted as ω, while the scattering angle (detector angle) is 2θ. The specular condition (for a flat surface) is fulfilled, when $\mathbf{k}_f$ leaves the surface also at an angle ω, i.e. for $\theta = \omega$. The scattering vector $\mathbf{q} = \mathbf{k}_f - \mathbf{k}_i$ then is parallel to $\mathbf{z}$. For the experiments presented here, both the magnetic field $\mathbf{H}$ and the axial pressure p were applied normal to the scattering plane.

index of refraction for the neutrons:

$$n = \sqrt{1 - V/E} := 1 - \delta \tag{1}$$

$$\approx 1 - V/2E, \qquad \text{for } V/2E \ll 1 \tag{2}$$

with the neutron energy $E = E^{\text{kin,vacuum}} = m_\text{n} v^2/2 = 2\pi^2\hbar^2/m_\text{n}\lambda^2$, and the scattering potential V experienced by the neutrons. The latter contains the nuclear potential $V^\text{nuc} \propto \rho^b$ (the laterally averaged neutron scattering length density) and the magnetic scattering potential $V^\text{mag} = \boldsymbol{\mu}_\text{n}\mathbf{B}_\perp$ with the components of the magnetic induction $\mathbf{B}$ normal to the scattering vector $\mathbf{q}$ and the neutron magnetic moment $\boldsymbol{\mu}_\text{n}$. By substituting for (depth dependent) material properties and neutron wavelength λ for V and E, one obtains:

$$\delta(z) = \underbrace{\frac{\lambda^2}{2\pi}\overbrace{\sum_i \rho_i(z) b_i}^{\rho^b(z)}}_{\delta^\text{nuc}(z)} + \underbrace{\frac{\lambda^2}{2\pi}\cdot\frac{-m_\text{n}}{2\pi\hbar^2}\boldsymbol{\mu}_\text{n}\mathbf{B}_\perp(z)}_{\delta^\text{mag}(z)} \tag{3}$$

with the number density ρ_i and the nuclear scattering length b_i, where the index i runs over all isotopes. Both, δ^nuc and (if present) δ^mag are of the order of 10^{-7} to 10^{-6}, which justifies the step from eqn. 1 to eqn. 2. Since only δ^mag depends on the neutron spin polarisation, it is possible to extract $\mathbf{B}_\perp$ from the reflectivities for both neutron polarisations:

$$B_\perp = \frac{2\pi\,\hbar^2}{m_\text{n}\mu_\text{n}}\cdot\frac{\delta^\text{mag}}{\lambda^2/2\pi} \approx \frac{\delta^\text{mag}}{\lambda^2/2\pi}\,4.318\cdot 10^{-15}\,\text{m}^2\,\text{T}. \tag{4}$$

The index $\perp$ of $\mathbf{B}_\perp$ indicates, that only the components normal to the scattering vector $\mathbf{q}$ are relevant. This still leaves a degree of freedom for the direction of $\mathbf{B}_\perp$ relative to the magnetic moment $\boldsymbol{\mu}_\text{n}$ of the neutrons. $\boldsymbol{\mu}_\text{n}$ is either parallel (spin up, $+$) or antiparallel (spin down, $-$) to the externally applied magnetic field $\mathbf{H}$. In most cases (including the present one) $\mathbf{H}$ is chosen to be normal to the scattering plane (see Figure 1). The component of $\mathbf{B}_\perp$ parallel to $\boldsymbol{\mu}_\text{n}$ leads to scattering which preserves the neutron spin state, while the perpendicular component (also in the sample plane) causes a flip of the spin and thus gives rise to so-called spin-flip scattering. Accordingly, it is possible to determine the orientation of $\mathbf{B}$ relative to the known neutron spin direction by measuring the non-spin flip signals R_{++} and R_{--} as well as the spin flip signals denoted by R_{+-} and R_{-+}. The absence of spin flip scattering

shows that the magnetic moments in the film plane are predominantly parallel to $\boldsymbol{\mu}_\mathrm{n}$ and the external field $\mathbf{H}$.

In analogy to the nuclear term in eqn. 3 one can define $\delta^\mathrm{mag} := \lambda^2/2\pi \cdot \sum_j \rho_j p_j$ with the magnetic scattering lengths p_j. The index j runs over all non-symmetry equivalent atoms (in contrast to i in b_i, which disregards symmetry, but differentiates the isotopes). If one assumes that the magnetic moments can be assigned to a single lattice site j, the following Ansatz is possible:

$$\mathbf{B} = \rho_j \mu_0 \boldsymbol{\mu}_j \tag{5}$$

$$= \rho_j \mu_0 \mu_\mathrm{B} g\, \mathbf{s}_j \tag{6}$$

with the effective magnetic moment $\boldsymbol{\mu}_j$ which can be expressed as an effective spin $\mathbf{s}_j$ times the Landé g-factor and the Bohr magneton. [1, p.311] Thus, using eqn. 4,

$$g\, s_j = \frac{B}{\mu_0 \mu_\mathrm{B} \rho_j} \tag{7}$$

$$= \frac{2\pi\, \hbar^2}{\rho_j\, m_\mathrm{n} \mu_\mathrm{n} \mu_0 \mu_\mathrm{B}} \frac{\delta^\mathrm{mag}}{\lambda^2/2\pi} \tag{8}$$

$$\approx \frac{1}{\rho_j} \frac{\delta^\mathrm{mag}}{\lambda^2/2\pi}\, 3.705 \cdot 10^{14}\, \mathrm{m}^{-1} \tag{9}$$

gives the moment per magnetic ion j in multiples of μ_B.

To probe the depth profile of the potentials discussed so far, one uses the following effect: An incoming wave field $\mathbf{k}_\mathrm{i}$ impinging on an ideal interface separating media with different indices of refraction at an angle ω is partly reflected into $\mathbf{k}_\mathrm{f}$ (also with an angle ω) and partly transmitted. The reflectivity decays approximately as q^{-4} for q_z much larger than the critical scattering vector for total reflection q_c. This has the consequence that the signal reaches the background level rather soon: Typical dynamic ranges of the measured intensity are 4 to 7 orders of magnitude, corresponding to $q_z \approx 2$ to $10\,\mathrm{nm}^{-1}$. For the derivation of the reflectance and refraction please refer to [2]. If several coplanar interfaces are present, multiple scattering leads to wave fields propagating through the sample, as is illustrated in Fig. 2. The interference of all components that leave the uppermost interface is a function of the angle of incidence ω, the wavelength, and the depth profile $V(z)$. By varying either ω (angle dispersive reflectometry) or λ (energy dispersive reflectometry) and measuring the intensity of the reflected beam one obtains the reflectivity $R(q_z)$ with $q_z = |\mathbf{k}_\mathrm{f} - \mathbf{k}_\mathrm{i}| =$

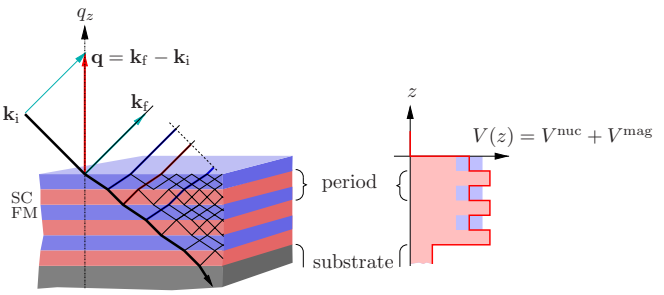

FIG. 2: Sketch to illustrate the wavefields formed in a multilayer by refraction and multiple reflection at the interfaces (*left*); and the corresponding depth profile of the potential V (*right*). The red solid line in the depth profile stands for the nuclear contribution, the shaded areas mark the potential including magnetic contributions for $|-\rangle$ (*red*) and $|+\rangle$ neutrons (*red* and *blue*).

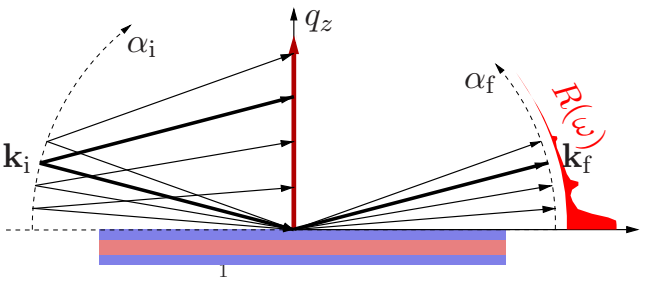

FIG. 3: Illustration of the angle dispersive measurement mode.

$4\pi \sin\omega/\lambda$. Fig. 3 illustrates the measurement with an angle dispersive mode. In that case, the angle ω is sometimes referred to as α_i and the angle of the reflected beam is referred to as α_f.

A periodic stack of materials gives rise to constructive and destructive interferences. The corresponding maxima are often called "Bragg peaks" even though Braggs law usually does not include refraction effects: Total external reflection shifts the Bragg condition and the inclination of the internal beam for small angles leads to compression of the peak distances relative to the refraction-free case. This explanes the non linearity of the scales of q_z and the inverse layer thickness.

EXCLUSION OF SMALL ANGLE SCATTERING AS ORIGIN OF THE FRACTIONAL PEAK:

In order to rule out small angle scattering from the $SrTiO_3$ substrate as the origin of the fractional peak, we performed measurements with an area detector in time-of-flight (TOF) mode. In fig 4 the result is shown after converting position to angle 2θ and time to wavelength λ. The bright horizontal band at $2\theta = 0$ originates from the direct beam. Neutrons reflected specularly from a flat surface would result in a single intensity stripe at constant 2θ, where θ is the angle of incidence of the neutron beam. Our observation of a bundle of stripes in the range $0.5° < 2\theta < 1.4°$ indicates that the surface consists of flat facets, tilted relative to each other by approximately $0.05°$.

In the chosen representation constant $q_z = 4\pi \sin\theta/\lambda$ values fall on a line through the origin. This is most pronounced for the edge of total external reflection but also the corresponding first Bragg peaks (weak dots at small λ) are positioned on such sharp lines.

For two of the facets corresponding to $2\theta = 0.85°$ and $0.95°$ (marked by the arrow) the fractional peaks can be most clearly seen.

If not caused by a highly periodic density modulation, small angle scattering origination from the substrate or the film should peak at $2\theta = 0$ and fall off continuously to larger angles. Such a behaviour can be seen for $\lambda < 3.5$ Å.

Even if the substrate shows a periodic pattern, the small angle scattering should be symmetric around $2\theta = 0$. Since the signal for negative 2θ is completely missing, the origin of the signal at the fractional-order Bragg-peak position must be due to a periodic modulation of the scattering potential of the YPBCO/LCMO film.

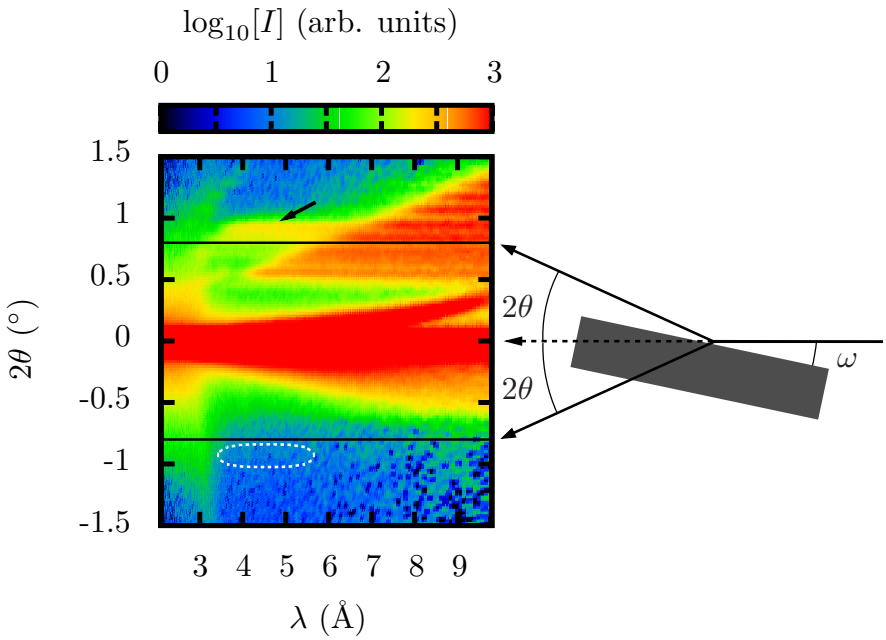

FIG. 4: Neutron measurement in time of flight mode with an area detector. The neutron wavelength is plotted versus the scattering angle 2θ. If the fractional peak (indicated by the arrow) would be originating from small angle scattering, the main intensity should be located at $2\theta = 0$ and fall off continuously to larger angles. It should further be symmetric towards positive and negative 2θ-values (at the see marked area at negative 2θ-values). Therefore, small angle scattering can be excluded as the origin of the SC-induced signal at the fractional order Bragg peak position.

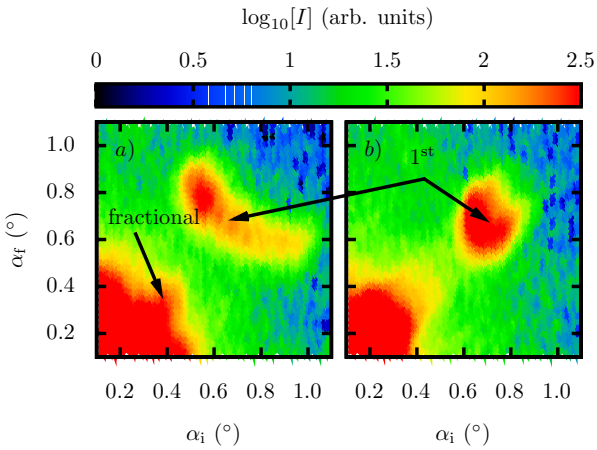

FIG. 5: Orientation dependence of the fractional-order superlattice Bragg reflex measured at 15 K in $H_{\mathrm{appl}} = 100\,\mathrm{Oe}$. The sample is rotated by 90° around its surface normal, the geometries with the scattering plane parallel to the (100) and the (010) directions of the $SrTiO_3$ substrate are denoted as the a- and b-directions, respectively. The angle of the incident beam α_{i} is plotted versus the angle of the scattered beam α_{f}. The colour scale is given by the logarithm of the measured intensity. The rocking scans ($\alpha_{\mathrm{i}} + \alpha_{\mathrm{f}} = \mathrm{const}$) are broad along the a-direction and narrow along the b-direction. This establishes a strongly anisotropic domain pattern of predominantly structural origin which involves a tilting of the substrate surface of up to 0.5° that persists throughout the entire superlattice [3]. The fractional superlattice Bragg reflex is only visible along the a-direction as indicated by the arrow.

ADDITIONAL NEUTRON MEASUREMENTS ON THE $[Y_{0.6}PR_{0.4}BA_2CU_3O_7$ (10 NM)/$LA_{2/3}CA_{1/3}MNO_3$ (10 NM)$]_{10}$ SUPERLATTICE:

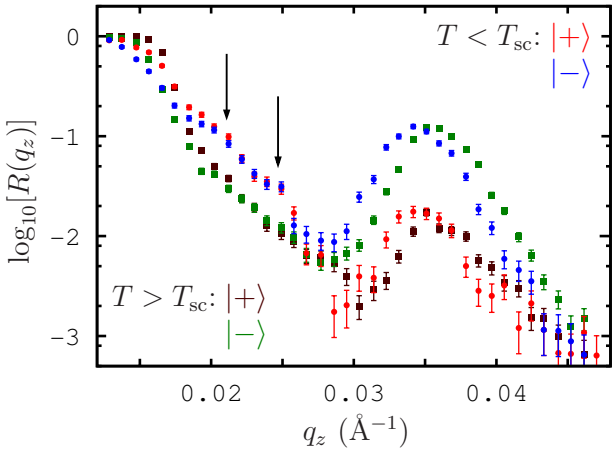

FIG. 6: Polarized specular neutron reflectivity curves in a-axis orientation as obtained on the same $[Y_{0.6}Pr_{0.4}Ba_2Cu_3O_7$ (10 nm)/$La_{2/3}Ca_{1/3}MnO_3$ (10 nm)$]_{10}$ superlattice that is discussed in the letter. The measurements were performed with the same setup at the Morpheus beamline at SINQ as the ones for which the spectra are shown in Figure 2 and 3 of our letter. The only obvious difference concerns the mounting of the sample which was pressed to an aluminum sample holder by means of a spring whose tension was not well controlled in the present case. While in Fig. 2 and 3 of our letter the SC-induced fractional superlattice Bragg peaks appear either at $q_z \approx 0.022\,\text{Å}^{-1}$ or at $q_z \approx 0.025\,\text{Å}^{-1}$, both of these SC-induced peaks can be seen to appear simultaneously (as indicated by the arrows).

CORRESPONDING NEUTRON REFLECTIVITY MEASUREMENTS ON A SECOND $[Y_{0.6}PR_{0.4}BA_2CU_3O_7$ (8.5 NM)/$LA_{2/3}CA_{1/3}MNO_3$ (8.5 NM)$]_{13}$ SUPERLATTICE:

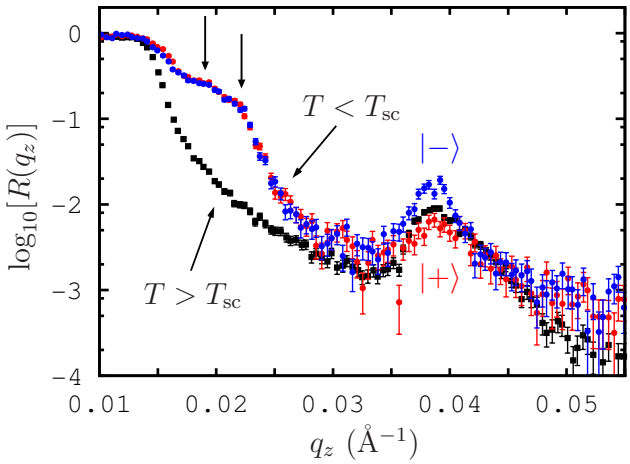

FIG. 7: Neutron reflecticity spectra in a-axis orientation for a second, $[Y_{0.6}Pr_{0.4}Ba_2Cu_3O_7$ (8.5 nm)/$La_{2/3}Ca_{1/3}MnO_3$ (8.5 nm)$]_{13}$, superlattice with $T_{sc} \approx 40$ K. Shown are representative spectra at $T > T_{sc}$ (unpolarized, black line) and at $T < T_{sc}$ spin up (*red*, $|+\rangle$) and spin down (*blue*, $|-\rangle$). Prominent SC-induced fractional order superlattice peaks (marked by the arrows) can be seen to develop also in this sample. Note that the 1st Bragg reflex is at a different q_z value (0.038 Å^{-1}), since the individual layers are 8.5 nm instead of 10 nm thick.

ADDITIONAL INTERPRETATION:

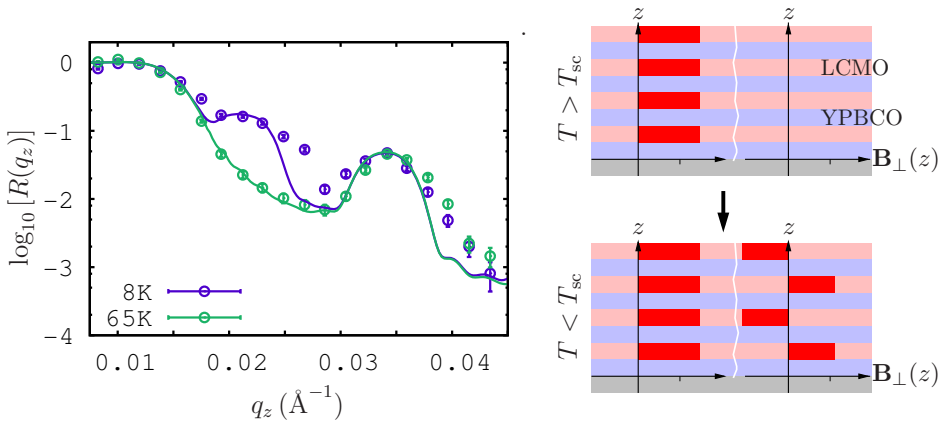

FIG. 8: a) Simulations (lines) of the unpolarised neutron reflecticity spectra at 65 and 8 K (the same as shown in Fig. 2a of our letter) of the $[Y_{0.6}Pr_{0.4}Ba_2Cu_3O_7$ (10 nm)/$La_{2/3}Ca_{1/3}MnO_3$ (10 nm)$]_{10}$ superlattice. Error bars show statistical errors. b) Sketch of the block-like model potential which assume an inhomogeneous spatial (domain-like) distribution of the magnetic potentials and their SC-induced variation. It is assumed here that for 60% of the superlattice volume the magnetic potential remains constant with the same average magnetization of 3.7 μ_B per Mn ion in every LCMO layer. This component accounts for the 1st order superlattice Bragg-peak whose intensity hardly changes around $T_{sc} = 40$ K. The remaining 40% of the LCMO domains are either anti-ferromagnetic or paramagnetic at $T > T_{sc}$ while they become FM at $T < T_{sc}$. In the SC state the average FM moment per LCMO layer is 2.8 μ_B per Mn ion, the direction alternates along the superlattice direction. This second component yields the fractional order superlattice Bragg peak which appears only in the SC state. Evidently, this domain state model yields a similarly good fit to the experimental data as the laterally homogeneous model that is presented in Fig. 2 of our letter. However, as mentioned in the letter, we believe that this model is fairly unrealistic since FM order in the LCMO layers needs to occur concurrently with the onset of SC in the YPBCO layers.

[1] Bland, J.A.C. and Heinrich, B. *Ultrathin Magnetic Structures.* 2 (Springer 1994).

[2] Daillant, J. and Gibaud, A. *X-Ray and Neutron Reflectivity: Principles and Applications*, Lecture Notes in Physics m 58 (Springer, 1999).

[3] Hoppler J., Stahn J., Bouyanfif H., Malik V.K., Patterson B.D., Willmott P.R., Cristiani G., Habermeier H.-U., and Bernhard C., *X-ray study of structural domains in the near-surface region of* $SrTiO_3$ *substrates with* $Y_{0.6}Pr_{0.4}Ba_2Cu_3O_7/La_{2/3}Ca_{1/3}MnO_3$ *superlattice grown on top.* Phys. Rev. B **78**, 134111 (2008).